Mon. Not. R. Astron. Soc. **340,** 923–936 (2003)

Three-dimensional convection simulations of the outer layers of the Sun using realistic physics

F. J. Robinson,[1]★ P. Demarque,[1] L. H. Li,[1] S. Sofia,[1] Y.-C. Kim,[2] K. L. Chan[3] and D. B. Guenther[4]

[1]*Astronomy Department, Yale University, Box 208101, New Haven, CT 06520-8101, USA*
[2]*Yonsei University, Seoul, South Korea*
[3]*Hong Kong University of Science & Technology, Hong Kong, China*
[4]*Department of Astronomy and Physics, Saint Mary's University, Halifax, Nova Scotia B3A 4R2, Canada*

Accepted 2002 December 11. Received 2002 December 2; in original form 2002 September 11

ABSTRACT

This paper describes a series of three-dimensional simulations of shallow inefficient convection in the outer layers of the Sun. The computational domain is a closed box containing the convection–radiation transition layer, located at the top of the solar convection zone. The most salient features of the simulations are that: (i) the position of the lower boundary can have a major effect on the characteristics of solar surface convection (thermal structure, kinetic energy and turbulent pressure); (ii) the width of the box has only a minor effect on the thermal structure, but a more significant effect on the dynamics (rms velocities); (iii) between the surface and a depth of 1 Mm, even though the density and pressure increase by an order of magnitude, the vertical correlation length of vertical velocity is always close to 600 km; (iv) in this region the vertical velocity cannot be scaled by the pressure or the density scaleheight; this casts doubt on the applicability of the mixing length theory, not only in the superadiabatic layer, but also in the adjacent underlying layers; (v) the final statistically steady state is not strictly dependent on the initial atmospheric stratification.

Key words: convection – methods: numerical – Sun: atmosphere – Sun: interior.

1 INTRODUCTION

It is now just possible to perform physically realistic three-dimensional (3D) simulations of the surface layers of the Sun, which take into account the complex interaction between radiative and convective energy transport (Kim & Chan 1998; Stein & Nordlund 1998 hereafter denoted as KC and SN, respectively, Stein & Nordlund 2000). There have also been a number of two-dimensional (2D) simulations of the surface layers (Steffen et al. 1990; Gadun et al. 2000). To model solar convection realistically requires a realistic equation of state, realistic opacities and a proper treatment of radiative transfer in the shallow layers. SN and KC are the two most frequently cited 3D models with this type of stratified convection. As their approaches differ considerably, both in numerical methods and in input model physics, it is important to find out what particular aspect of the respective simulations caused their results to be different.

The aim of this paper is to describe solar surface convection that not only has the KC realistic physics, but also has a realistic (as far as is presently possible) geometry. To achieve this we had to increase both the depth and width of the original KC model, until the side walls and the horizontal boundaries had only a minimal effect on the flow. The simulations themselves model a region less than a few thousand kilometres in depth, as measured inwards from the visible solar surface. In the deep regions of the solar convection zone, the turbulent velocity is subsonic and the superadiabaticity is close to zero. However, within a few hundred kilometres of the solar surface, the convective flux starts to decrease. As the total flux is constant, the radiative flux must increase to offset the drop in the convective flux. This is achieved by a rise in the local temperature gradient ∇. This region of inefficient convection is called the superadiabatic layer (SAL). In the SAL, the superadiabaticity $\nabla - \nabla_{\rm ad}$ is positive and of the order of unity (Demarque, Guenther & Kim 1997, 1999). As the buoyancy force is large in the SAL, the region is characterized by highly turbulent velocities and large relative thermodynamic fluctuations. The turbulent velocity also gives rise to a significant turbulent pressure (approximately 15 per cent of the gas pressure). This moves out the convection surface, modifying the SAL and the stratification. In one-dimensional (1D) models of the solar convection zone based on the mixing length theory (MLT) (Böhm-Vitense 1958), the velocity is set to zero above the convection boundary. However, 3D numerical simulations described in Cattaneo, Hurlbert & Toomre (1990), have shown that just

★E-mail: marjf@astro.yale.edu

above the top of the convection layer the turbulent velocities are still high.

There are several motivations for such simulations among stellar physicists. One is to understand the effects of turbulence on the structure of the outer solar layers as revealed by the observed frequencies of solar p-modes. Another is to explain the excitation mechanism of the p-modes. Still another is to derive more realistic surface boundaries for stars with convection zones from first physical principles, free of the arbitrary assumptions of the mixing length theory. And finally, such simulations may be of help in investigations of the solar dynamo.

Over the previous few years, the science of helioseismology has provided some very precise measurements of the p-mode oscillation frequencies (to within one part in 1000) in the surface layers of the Sun (Harvey et al. 1996). The discrepancy between the observed p-mode frequencies and those calculated from solar models, is known to be primarily caused by the approximations made in modelling the surface layers, where turbulent and radiative losses are significant (Balmforth 1992; Guenther 1994). In the 3D simulation described in KC, the turbulent pressure pushed the convective boundary radially outwards from its original position (which was computed using the MLT). This situation was mimicked in the 1D solar model by tweaking the opacity in the outer layers (Demarque et al. 1999). This resulted in improved p-mode frequencies for low and intermediate degrees. However, Demarque et al. also showed that the mixing length prescription of Canuto & Mazzitelli (1991), which had a completely different SAL structure than KC, could produce a similar improvement of the p-mode frequencies for the same l-values. Full details of the different approaches, the contrasting SAL structures and the resulting p-modes, are described in Demarque et al. (1997, 1999). Later, Rosenthal et al. (1999) used another approach to compute the p-mode frequencies. These authors patched the mean stratification (horizontal average) of a 3D hydrodynamical simulation, on to a 1D MLT envelope model. In order to obtain a smooth 1D model, they adjusted the mixing length and the amplitude of the turbulent pressure to match the 3D simulation. The computed frequencies were closer to the observed frequencies than if a standard solar model had been used, thus showing the importance of including turbulence in modelling the outer layers of the Sun. More recently, Li et al. (2002) found similar results to Rosenthal et al. by inserting the averaged turbulent pressure and turbulent kinetic energy directly into the 1D stellar model. Their method is applied to two of the simulations described in this paper (see Section 4.3). As the turbulent kinetic energy and turbulent pressure were very small at the base of the 3D model, they were set to zero in regions of the 1D stellar model that lay below the 3D model domain. This required the usual adjustment of the mixing length parameter and the helium abundance to calibrate the perturbed stellar model. No other adjustable parameters were employed. The improvement in the eigenfrequencies was found to be primarily caused by the inclusion of turbulent kinetic energy in the 1D stellar model.

After extensive testing, we found that our simulations are in good agreement with other numerical studies of the surface layers (e.g. Rosenthal et al. 1999; Asplund et al. 2000). In addition, by incorporating the computed 3D turbulence into a 1D stellar model, we were able to produce solar surface eigenfrequencies (p-modes) that were very close to the observed frequencies. As our eventual goal is to simulate the SAL in stars other than the Sun, it is vital to be sure we are modelling the Sun as correctly as possible.

2 MODELLING REALISTIC SOLAR SURFACE CONVECTION

To model surface layer convection in the Sun as realistically as possible, we take the following approach.

(i) Using a stellar evolution code (YREC, e.g. see Guenther et al. 1992), we compute a standard stellar model from which the initial density ρ and internal energy e, required by the 3D simulations, are derived. From an arbitrary initial velocity field $\boldsymbol{v}$, we then compute ρ, E $(=1/2\rho v^2 + e)$, ρv_x, ρv_y and ρv_z. These are the dependent variables of the governing equations. The horizontal directions are x and y, and z is radially outwards.

(ii) Using the same tables for the equation of state and the opacities as in the stellar model, we then compute the pressure $P(\rho, e)$, temperature $T(\rho, e)$, Rosseland mean opacity $\kappa(\rho, e)$, specific heat capacity at constant pressure $c_p(\rho, e)$, adiabatic gradient $\nabla_{\rm ad}(\rho, e)$ and some thermodynamic derivatives.

(iii) The radiation flux is then computed using the diffusion approximation in the optically thick regions and the 3D Eddington approximation in the optically thin layers.

(iv) We then integrate the Navier–Stokes equations over one time-step to compute a new set of dependent variables and return to (ii).

2.1 Realistic initial conditions: steps (i) and (ii)

The solar model uses the same realistic physics as described in Guenther & Demarque (1997). In particular, the low-temperature opacities of Alexander & Ferguson (1994) and the OPAL opacities and equation of state were used (Iglesias & Rogers 1996). Hydrogen and helium ionization, and the diffusion of both helium and heavy elements are included.

In the initial model, the atmospheric layers, which are in radiative equilibrium, are assumed to be grey. Deeper in, in the convectively unstable region, the thermal structure is described by the MLT, which prescribes the temperature gradient ∇. In the original KC simulation, the Eddington approximation $T(\tau)$ relation was used in the atmosphere. In this case, the values of the parameters, X, Z and α, in the calibrated standard solar model (SSM) are $(X, Z, \alpha) = (0.7385, 0.0181, 2.02)$, where X and Y are the hydrogen and helium abundances by mass, and α is the ratio of the mixing length to the pressure scaleheight (PSH) in the convection zone, required to match the solar radius precisely. It should be mentioned that although the values of X and Y in the calibrated SSM depend little on the treatment of the surface layers, the value of α is sensitive to the choice of the $T(\tau)$ relation in the atmosphere (Guenther et al. 1992).

We note that for simulations discussed in this paper (those listed in the appendix), the empirical Krishna–Swamy $T(\tau)$ relation for the Sun (Krishna Swamy 1966) was used instead of the Eddington approximation. The same model as KC, but constructed with the Krishna–Swamy $T(\tau)$ relation, yields $(X, Z, \alpha) = (0.7424, 0.017\,06, 2.1319)$ (this is model KC2 in the appendix). Because of the inclusion of helium and heavy element diffusion during the evolution, the initial X and Z (denoted by $X0$, $Z0$) were slightly different. For KC they were $(X0, Z0) = (0.7066, 0.0201)$, and for KC2 they were $(X0, Z0) = (0.710, 0.019)$. The difference in initial atmospheric structures between simulations KC and KC2 provides us with the opportunity to verify that the final state in the simulations is not strictly dependent on the choice of $T(\tau)$ relation in the initial model. This important test is discussed in the appendix.

For each time-step of the numerical integration we need to solve the complex equation of state (step ii). This adds considerable computational time compared with an ideal simulation, such as with a perfect gas. The 3D hydrodynamical simulations use identical opacities and equation of state to that used in the 1D reference SSM, which served as the initial model. The side boundaries are periodic, while the top and bottom boundaries are stress-free. A constant heat flux flows through the base and the top is a perfect conductor. To ensure that mass, momentum and energy are fully conserved, we use impenetrable (closed) top and bottom boundaries.

A particular model is specified by g (the surface gravity) and $T_{\rm eff}$ (the effective temperature). Aside from the viscosity coefficients there are no other free parameters.

2.2 Radiative transfer: step (iii)

In the SAL, the photon mean free path may not be small enough to use the diffusion approximation. Consequently, one is forced to either solve the full radiative transport equation or consider the three-dimensional Eddington approximation (Unno & Spiegel 1966), which is a higher-order approximation than the diffusion approximation, and is valid in the optically thin regions. Computationally, to solve the full radiative transport equations is formidable, and only a few ray directions are currently used in this approach (SN). In our simulations, we have chosen to use the three-dimensional Eddington approximation.

In the deeper part of the domain ($\tau > 10^4$), we use the diffusion approximation,

$$Q_{\rm rad} = \nabla \cdot \left[\frac{4acT^3}{3\kappa\rho} \nabla T \right], \tag{1}$$

where κ is the Rosseland mean opacity, a is the Boltzmann constant and c is the speed of light. In the shallow region $Q_{\rm rad}$ is computed as

$$Q_{\rm rad} = 4\kappa\rho(J - B), \tag{2}$$

where the mean intensity J was computed using the generalized three-dimensional Eddington approximation (Unno & Spiegel 1966),

$$\nabla \cdot \left(\frac{1}{3\kappa\rho} \nabla J \right) - \kappa\rho J + \kappa\rho B = 0, \tag{3}$$

where B is the Planck function. This formulation is exact for isotropic radiation in a grey atmosphere, and without requiring local thermodynamic equilibrium, the Eddington approximation describes the optically thick and thin regions exactly (Rutten 1995). To study spectral line profiles and the spectral energy distribution requires a frequency-dependent radiative transfer. However, in a study of the SAL, to serve as a surface boundary condition for stellar models or for comparison with the results of helioseismology, we found a grey atmosphere to be adequate.

2.3 Hydrodynamics: step (iv)

For deep ($v \ll c_{\rm s}$, where v is the flow velocity and $c_{\rm s}$ is the isothermal speed of sound) and efficient ($\nabla - \nabla_{\rm ad}$ just above zero) convection, Chan & Sofia (1989) showed that the MLT is a very good approximation to the real situation. However, in the SAL, both $v/c_{\rm s}$ and $\nabla - \nabla_{\rm ad}$, can be of the order of unity. In this case, the MLT is unlikely to apply. The validity of this argument is confirmed by helioseismology. The run of the speed of sound in the SAL derived by inversion of the helioseismic data does, in fact, disagree with the MLT model (Basu & Antia 1997). In such an environment, the governing hydrodynamic equations are the fully compressible Navier–Stokes equations (see, for example, Kim et al. 1995).

$$\partial\rho/\partial t = -\nabla \cdot \rho\boldsymbol{v} \tag{4}$$

$$\partial\rho\boldsymbol{v}/\partial t = -\nabla \cdot \rho\boldsymbol{v}\boldsymbol{v} - \nabla P + \nabla \cdot \boldsymbol{\Sigma} + \rho\boldsymbol{g} \tag{5}$$

$$\partial E/\partial t = -\nabla \cdot [(E + P)\boldsymbol{v} - \boldsymbol{v} \cdot \boldsymbol{\Sigma} + \boldsymbol{f}] + \rho\boldsymbol{v} \cdot \boldsymbol{g} + Q_{\rm rad}, \tag{6}$$

where $E = e + \rho v^2/2$ is the total energy density and ρ, $\boldsymbol{v}$, P, e and $\boldsymbol{g}$, are the density, velocity, pressure, specific internal energy and acceleration owing to gravity, respectively. $Q_{\rm rad}$ is the energy transferred by radiation (see the previous section) and $\boldsymbol{f}$ is the diffusive flux. Ignoring the coefficient of bulk viscosity, the viscous stress tensor for a Newtonian fluid is $\Sigma_{ij} = \mu(\partial v_i/\partial x_j + \partial v_j/\partial x_i) - 2\mu/3(\nabla \cdot \boldsymbol{v})\delta_{ij}$, where μ is the dynamic viscosity and δ_{ij} is the Kronecker delta tensor.

In fully developed turbulence the ratio of the length of the largest eddy to the dissipation length is $\mathrm{Re}^{3/4}$, where Re is the Reynolds number (Landau & Lifshitz 1987). In the Sun, Re is of the order of 10^{12}, which means approximately 10^9 scales per dimension. A 3D direct numerical simulation of the Sun would thus require approximately 10^{27} grid points!

The large-eddy simulation (LES) approach assumes that the small scales are independent of the resolved scales (large eddies) and can be parametrized as a diffusion process. In this case μ is an eddy viscosity defined in terms of the resolved velocity (Smagorinsky 1963),

$$\mu = \rho(c_\mu\Delta)^2(2\boldsymbol{\sigma} : \boldsymbol{\sigma})^{1/2}. \tag{7}$$

The colon inside the parentheses denotes tensor contraction of the rate of strain tensor $\sigma_{ij} = (\nabla_i v_j + \nabla_j v_i)/2$. The subgrid scale (SGS) eddy coefficient c_μ, is set to 0.2, the value for incompressible turbulence and $\Delta = (\Delta_x\Delta_y)^{1/2}\Delta_z$ is an estimate of the local mesh size. To handle shocks, μ is multiplied by $1 + C \cdot (\nabla \cdot \boldsymbol{v})^2$, where the constant C is made as small as possible, while still maintaining numerical stability. As μ is dependent on the velocity divergence, any large velocity gradients are smoothed out by the increased viscosity. If a shock occurs it is not resolved, but smeared out by a local increase in viscosity.

The diffusive flux $\boldsymbol{f} = -(\mu/\mathrm{Pr})\,T\nabla S$, where the horizontal mean of the entropy gradient $\nabla S \leqslant 0$, i.e. the convection zone and $\boldsymbol{f} = -(\mu c_p/\mathrm{Pr})\nabla T$, where the horizontal mean of $\nabla S \geqslant 0$, i.e. the radiation zone (the Prandtl number Pr is defined below). In the convection layer the SGS diffusive flux tends to smooth out entropy fluctuations and make the layer close to adiabatic (in analogy with turbulent mixing). The change in the form of the diffusive flux above the convection boundary is necessary because the SGSs should continue to transport heat radially outwards though the top of the box. Away from the horizontal boundaries, $\boldsymbol{f}$ is close to zero. At the base, $\boldsymbol{f}$ is equal to $\sigma T_{\rm eff}^4$, where σ is the Stefan–Boltzmann constant. The Prandtl number $\mathrm{Pr} = \nu/\kappa$, where ν is the kinematic viscosity and κ is the thermal diffusivity. In the simulations $\mathrm{Pr} = \frac{1}{3}$. Owing to the inclusion of radiative energy transport the effective Pr is actually much smaller and not constant.

3 NUMERICAL INTEGRATION: OBTAINING ACCURATE STATISTICS

To simulate the highly stratified SAL of the Sun we need to relax the initial layer and then compute accurate statistics. The former requires a long computation, while the latter a small time-step. In compressible hydrodynamics, however, with an explicit numerical

method, the time-step must be less than the time for a sound wave to traverse two adjacent grid points. This is known as the Courant–Friedrichs–Lévy (CFL) stability criterion. Because of these considerations the simulations were performed in two stages.

First, using an implicit code in which the time-step is restricted by the flow speed rather than the speed of sound, the initial hydrostatic layer was allowed to adjust its thermodynamical structure until it was close to hydrodynamic equilibrium. This *thermal adjustment* phase took at least 5 h of solar surface convection time.

Secondly, using a second-order accurate explicit code, quantities were averaged over a time that was long enough for the averages to be independent of the integration time. As the explicit time-step is approximately five times smaller than the implicit time-step, prior to statistical averaging, the code was run for a few thousand time-steps. This allowed the simulation to adjust to the new time-step. The *statistical convergence* took at least an hour of solar surface convection time.

3.1 Thermal adjustment

The implicit code was the alternating direction implicit method on a staggered grid (ADISM) developed by Chan & Wolff (1982). This code was used to relax the fluid to a self-consistent thermal equilibrium.

The entire layer was assumed to be relaxed when:

(i) the energy flux leaving the top of the box was within 5 per cent of the input flux at the base;
(ii) the horizontally averaged vertical mass flux was less than 10^{-4} g cm^{-2} s^{-1} at every vertical level;
(iii) the overall thermal structure did not change much over time;
(iv) and the maximum velocity in the box was roughly constant.

These criteria must be satisfied, before any useful statistical data can be gathered.

3.2 Statistical convergence

A second-order explicit method (Adams–Bashforth time integration) gathered the statistics of the time-averaged state. This code is much more accurate than ADISM, for example the mean energy flux leaving the top of the box was within 1 per cent of the input flux at the base. On a 667 MHz Alpha processor, each integration step on a 80 × 80 × 80 grid, required approximately 5 s of CPU time.

The time required for statistical convergence depends on the particular quantity being averaged. Conserved quantities converge very fast. For example, the horizontally averaged vertical mass flux was less than 10^{-5} g cm^{-2} s^{-1} after 5 min of solar time integration. On the other hand, rms velocities converged in a few eddy turnover times (at least 30 min of solar time). While second-order turbulent quantities, such as the horizontal Reynolds stress, took even longer to converge (at least 80 min of solar time).

3.2.1 Some statistical definitions

In a turbulent fluid a quantity q can be split into a mean and a fluctuating part,

$$q = \bar{q}(z) + q'(x, y, z, t). \tag{8}$$

The overbar represents a combined horizontal and temporal average, i.e.

$$\bar{q}(z) = \frac{1}{t_2 - t_1} \int_{t_1}^{t_2} \left[\frac{1}{(L_x L_y)} \int q \, \mathrm{d}x \, \mathrm{d}y \right] \mathrm{d}t. \tag{9}$$

t_1 is a time after the system has reached a self-consistent thermal equilibrium (the thermal adjustment time). L_x and L_y are the horizontal widths of the box in the x and y directions, respectively. The time required for statistical convergence is $t_2 - t_1$.

The rms value of a quantity q is defined as

$$q'' = \overline{q^2} - \bar{q}^2, \tag{10}$$

while the correlation coefficient of two quantities q_1 and q_2, is defined as

$$C[q_1' q_2'] = \frac{\overline{q_1 q_2} - \overline{q_1}\,\overline{q_2}}{q_1'' q_2''}. \tag{11}$$

As the simulations have periodic side boundaries, symmetry requires that

(i) $C[v_x' \, v_y'] = 0$
(ii) $v_x'' = v_y''$.

The run of v_x'' and v_y'' after 80 min of time integration is shown in Fig. 1. The closeness of the horizontal velocities confirms that the simulation is close to statistical convergence.

By examining many different simulations we found that the run of $C[v_x' \, v_y']$ is generally a much stricter test of convergence. Fig. 2

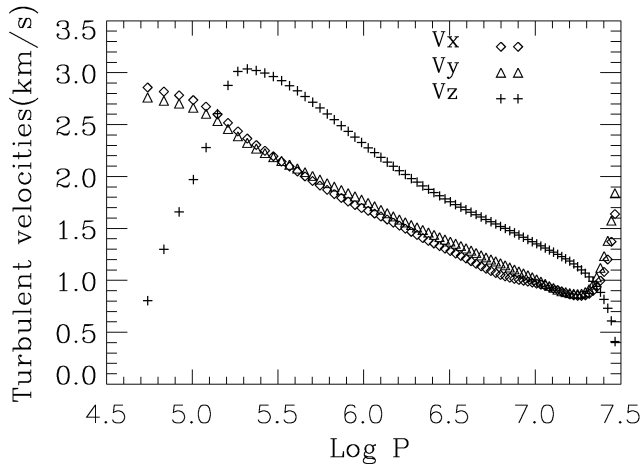

Figure 1. The rms turbulent velocities in the horizontal and vertical directions versus depth. The closeness of the two horizontal velocities confirms that the simulation is close to statistical convergence.

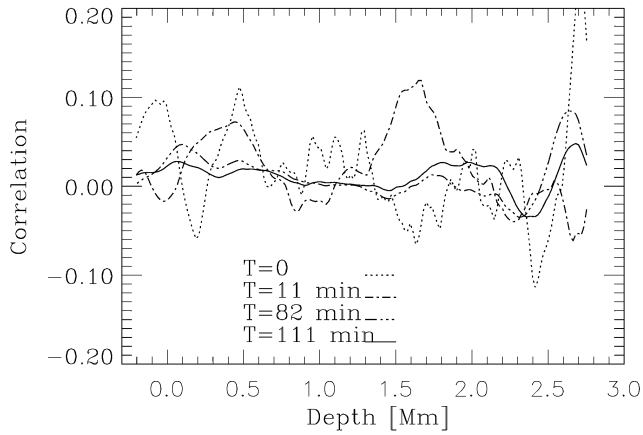

Figure 2. $C[v_x' \, v_y']$ for three integration times. As $C[v_x' \, v_y']$ converges more slowly than most other quantities, the degree of statistical convergence can be estimated by how close $C[v_x' \, v_y']$ is to zero. Convergence is slowest near the bottom of the box.

shows $C[v'_x\ v'_y]$ measured for four different integration times. Even after 80 min, $C[v'_x\ v'_y]$ is still approximately 0.1 near the bottom. Convergence is faster in the upper layers because when the convecting fluid elements move up through the stratification, their rapid expansion smooths out small-scale fluctuations.

4 MAIN RESULTS

4.1 Effect of domain size

After substantial numerical testing that is described in detail in the appendix, we found the following.

(i) An undesirable effect of the impenetrable horizontal boundary at the bottom was too speed up the overall flow. This produced an artificially high convective flux. Just below the surface the radiative flux is a significant fraction of the total flux. As the total energy flux is fixed, to accommodate the increased convective flux, the radiative flux had to reduce. This was achieved by an (unphysical) drop in the temperature gradient ∇ in the SAL region.

To avoid this, the lower boundary has to be positioned far enough away from the surface, so that the velocity at the base is small and uncorrelated from the motions near the surface.

(ii) If the width of the box was too small then the turbulent kinetic energy of the granules was artificially small. This is because the movement of the larger granules was restricted by the walls of the box.

To avoid this, the aspect ratio was doubled until the turbulent kinetic energy was unaffected by a further increase in aspect ratio. For the Sun this required a width of 2.7 Mm.

4.2 Comparison with previous 3D numerical simulations

4.2.1 Vertical velocity

Using the SN code, Asplund et al. (2000) computed a series of simulations of solar surface convection in a domain with a depth of approximately 4 Mm and a width of 6 Mm. The best resolution in Asplund et al. was $200^2 \times 82$. The rms vertical velocity and the mean velocity are shown in figs 3 and 4 in their paper. Corresponding velocity plots from our best model (model C in the Appendix) are shown in Fig. 3. Note that we have radially upwards as the positive

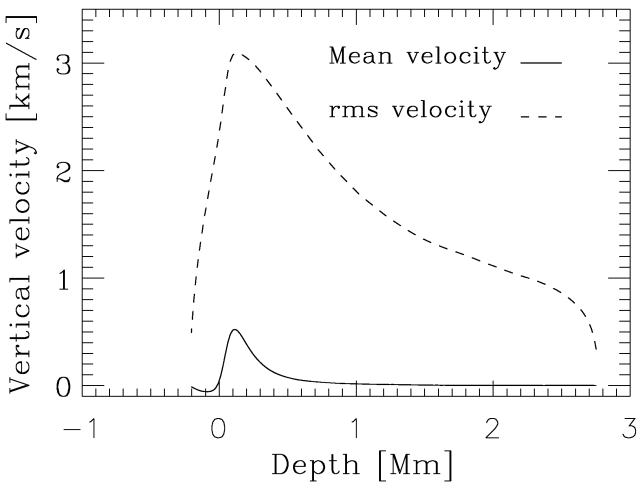

Figure 3. The mean and rms vertical velocity in model C.

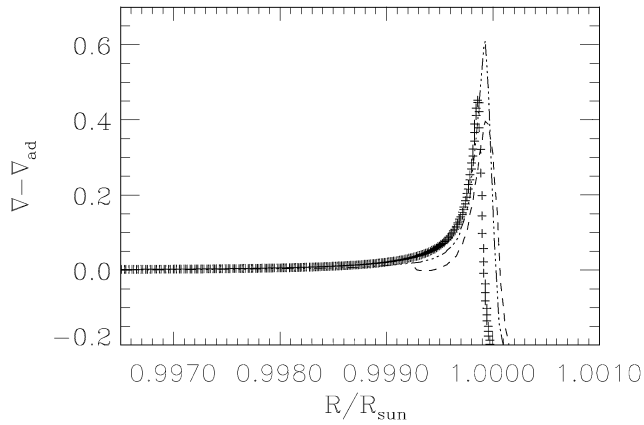

Figure 4. Superadiabaticity versus fractional radius. The crosses are from the 1D stellar model (MLT), the dashes are for model KC2 and the triple dot-dash line is for model C (see the Appendix for details). In both KC2 and C the original (MLT) convective boundary is moved out by turbulent pressure.

direction, which is opposite to Asplund et al.'s paper. Despite all the differences between the SN and KC approaches, away from the boundaries, the rms and mean vertical velocities in our best model are very similar to those in the best Asplund et al. simulation. The most noticeable differences occur at the top and bottom because in our simulations the vertical velocity is forced to drop to zero. In Asplund et al. the transmitting boundaries allowed the velocity to decrease more gently.

4.2.2 Superadiabaticity

The superadiabaticity $\nabla - \nabla_{\rm ad}$ for the MLT, and models KC2 and C, are plotted in Fig. 4. The abscissa is the radius of the simulation divided by the radius of the Sun. For model C, the superadiabaticity has a maximum of approximately 0.6, which is close to the value given by the SN code (see fig. 3 in Rosenthal et al.). The position of the top of the convection layer (as determined by the Schwarzschild criterion) was pushed out further in KC2 than in C. This is because of the higher turbulent pressure.

When the SAL was moved outwards the convective efficiency was reduced and radiation was forced to carry more of the total flux. This resulted in an increase in the height of the SAL in C (triple dot dashed line), compared with the MLT (crosses). However, in KC2 (dashed line) the convection was sped up by the lower boundary and thus is (incorrectly) more efficient than the MLT. This resulted in a drop in the height of the peak of the SAL compared with the MLT.

4.3 Comparison with observational results: *p*-mode oscillation frequencies

4.3.1 Implementation of 3D turbulence into 1D stellar models

By analogy with the work of Lydon & Sofia (1995) on magnetic effects, the 3D turbulence is parametrized in terms of two quantities (Li et al. 2002), the turbulent kinetic energy per unit mass,

$$\chi = \frac{1}{2} v''^2, \tag{12}$$

where $v''^2 = v''^2_x + v''^2_y + v''^2_z$ is a dimensional quantity, and an anisotropy parameter,

$$\gamma = 1 + 2(v_z''/v'')^2. \quad (13)$$

The z-direction is parallel to the radial direction.

The turbulence is included by incorporating two new variables γ and χ into the 1D stellar model. To understand how this works, consider a perfect gas in which the ratio of the specific heats $\gamma = c_p/c_v$, the internal energy $e = c_v T$ and the gas pressure $P = \rho RT$. The quantities c_v and R are for unit mass of a gas and T is the temperature. The previous three equations can be expressed as

$$\gamma = 1 + P/(\rho e). \quad (14)$$

If we replaced gas quantities by turbulent quantities, i.e. P by $P_{\rm turb}$ $(=\rho\, \overline{v_z''^2})$ and e by χ and rearrange, then we would obtain

$$P_{\rm turb} = (\gamma - 1)\rho\chi, \quad (15)$$

where γ is defined in terms of turbulent quantities (i.e. rms velocities). Including χ and γ is *equivalent* to including χ and $P_{\rm turb}$ in the 1D stellar model. The two variables γ and χ are included in the mathematical system in a self-consistent manner (see Li et al. for the full mathematical treatment)

For example, the equation of state for the 1D model becomes

$$\rho = \rho(P_T, T, \chi, \gamma),$$

where $P_T = P_{\rm gas} + P_{\rm rad} + P_{\rm turb}$.

The continuity equation and the equation of transport of energy by radiation remain the same regardless of turbulence. In terms of γ and χ, the hydrostatic equilibrium is

$$\frac{\partial P_T}{\partial M_r} = -\frac{GM_r}{4\pi r^4} - \frac{2(\gamma - 1)\chi}{4\pi r^3}, \quad (16)$$

where M_r, G and r have their usual standard stellar model (SSM) definitions. The energy conservation equation,

$$\frac{\partial L_r}{\partial M_r} = \epsilon - T\frac{\mathrm{d}S}{\mathrm{d}t}, \quad (17)$$

is also affected by the inclusion of χ, as

$$T\,\mathrm{d}S = \mathrm{d}U + (P_T - P_{\rm turb})\,\mathrm{d}(1/\rho) + \mathrm{d}\chi, \quad (18)$$

where $\mathrm{d}\chi$ represents the work performed by turbulence. The quantities L_r and ϵ have their usual SSM definitions.

The convective flux in the 1D model $F_{\rm conv} = \rho\ T\ DS\ V_{\rm conv}$ now includes the contribution from turbulent kinetic energy. $V_{\rm conv}$ is the MLT convective velocity and DS is the entropy excess. Equation (18) is the 'non-standard form' of the second law as described in Lydon & Sofia. As turbulence is, in general, anisotropic it is wrong to treat the work performed by turbulence as $-P_{\rm turb}\,\mathrm{d}V$. This is essentially because $P_{\rm turb}$ is a tensor and $P_{\rm gas}$ is a scalar.

The equation of energy transport by convection, does not change in form, but ∇ is different from that without turbulence. The equations that govern envelope integrations are changed accordingly (see Li et al.).

4.3.2 Solar p-mode oscillation frequencies

To investigate the effect of turbulence on the solar p-mode oscillation frequencies, the runs of χ and γ for models KC2 or C were incorporated into the 1D stellar model using the Li et al. method. For each run, the p-mode frequencies for $l = 0$, 1, 2, 3, 4, 10, ..., 100, were computed using Guenther's pulsation code (1994), under the adiabatic approximation. When comparing the computed and observed eigenfrequencies, one should really include the proper modelling of radiative gains and losses by computing the non-adiabatic frequencies (Guenther 1994). However, to help isolate the effects of turbulence on the p-mode frequencies, we computed the adiabatic frequencies. The difference between observed and computed adiabatic p-mode frequencies for the standard solar model is shown in Fig. 5. The frequency difference is scaled by the mode mass Q_{nl} (e.g. Christensen-Dalsgaard & Berthomieu 1991).

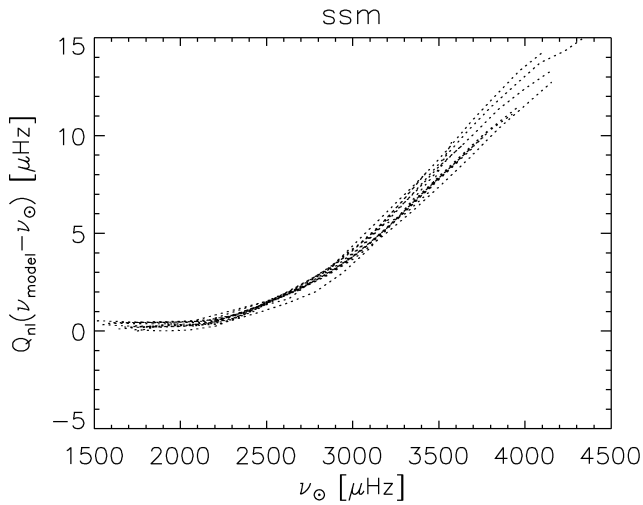

Figure 5. The difference between the observed and the computed p-mode frequencies for a standard solar model, SSM (see the text).

The Q_{nl} weighting attempts to correct the p-mode frequency differences, by removing the dependence on mode inertia. The mode differences with high mode inertia obtain more weight than those with lower inertia. This tends to give greater weight to the low-l, deep penetrating modes and less significance to the very high-l shallow modes. The result is the removal of the l dependence in the frequency differences owing to perturbations in the near surface regions. We are left with only an n dependence, which is equivalent to a frequency dependence. The Q_{nl} weighting enables us to see that the discrepancy between the observed and the computed adiabatic frequencies is worse at high frequencies, thus pointing to a problem in the surface layers. Without the Q_{nl} weighting, the mismatch would appear to a varying degree, at all frequencies and therefore it would not be as easy to claim that the outer layers are responsible for the mismatch.

In the statistically steady state (after the flow is thermally relaxed), the turbulent kinetic energy flux should be proportional to the energy input rate at the base. The turbulent kinetic energy χ should be independent of the geometry of the computational domain. If the box is too shallow or the width too narrow, then χ can be wrong. To illustrate the effect of the geometry on the frequencies, γ and χ from the KC2 model were used to compute a stellar model. The computed adiabatic frequencies with turbulence derived from KC2 are shown in Fig. 6. The resulting frequencies are much worse than the standard solar model. However, if we use model C instead of KC2, then the derived frequencies were improved considerably (Fig. 7). The difference between the computed and the observed frequencies is less than 5 μHz. The inclusion of turbulent kinetic energy in 1D models in addition to turbulent pressure, has a similar effect on the adiabatic frequencies to the inclusion of radiative losses/gains (computation of non-adiabatic frequencies). Both reduce the difference between the adiabatic frequencies and the observed frequencies by

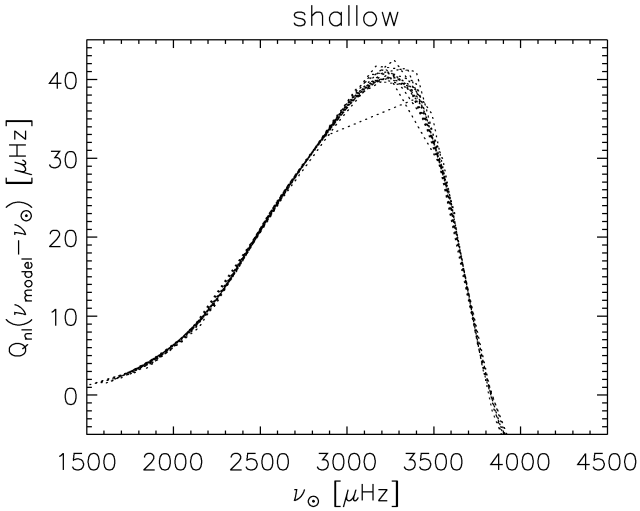

Figure 6. The difference between the observed and the computed p-mode frequencies for a solar model with turbulence included from model KC2 (see the Appendix).

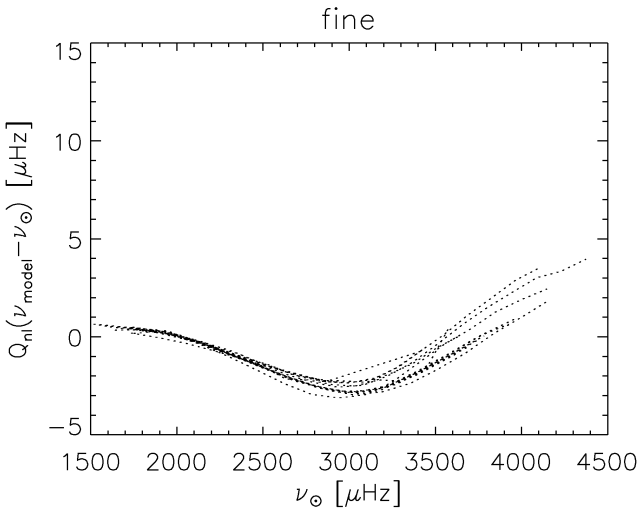

Figure 7. The difference between the observed and the computed p-mode frequencies with turbulence included from model C (see the Appendix).

an order of magnitude. This mean that the turbulent correction to the p-modes is as important as radiative losses/gains.

4.4 Characteristics of the solar granules

4.4.1 Size

Fig. 8 shows a set of contours of the instantaneous vertical velocity. From top to bottom the frames depict depths of −0.14, 0.03, 0.2 and 1.0 Mm. The depth was measured positively inward from the visible solar surface. The contours themselves have been derived from a simulation of 80^3 grid points, in a domain with a horizontal area of 3.75×3.75 Mm^2 and a depth of 2.5 Mm. At this instant in time there appear to be between three and four granules near the surface. The thick black lines represent the strong downflows that occur at the sides of the granules. The lighter regions denote upflowing fluid or weak downflows. The granular pattern seems to persist over the first three frames, suggesting that the granule structure is correlated

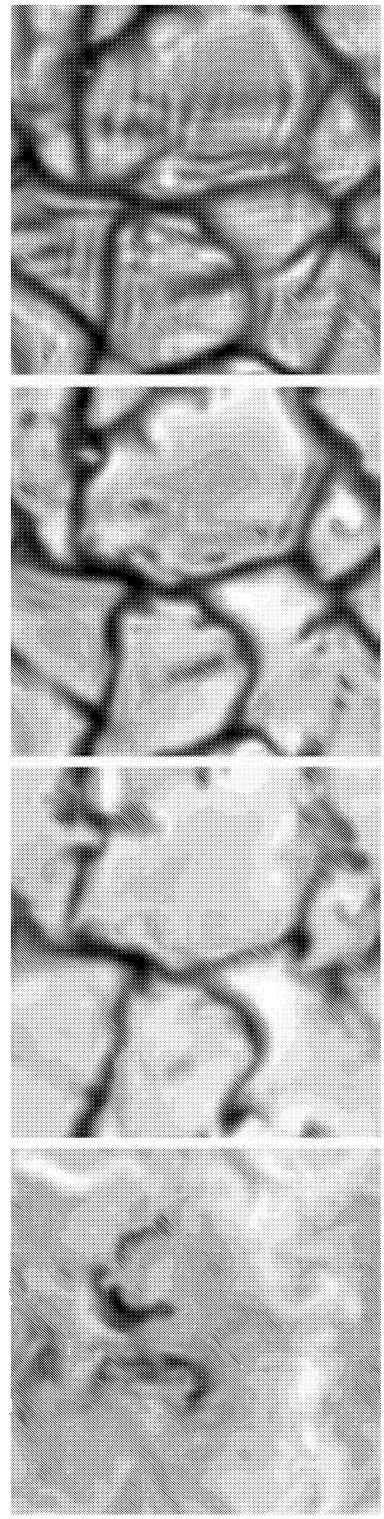

Figure 8. Contours of vertical velocity at one instant in time. The darker regions are downflows, and the lighter regions are upflows. From top to bottom, the frames are at depths of −0.14, 0.03, 0.2 and 1.0 Mm. Positive depths are measured inwards from the solar surface. The width of each frame is 3.75 Mm. The small parallel vertical lines in the first frame indicate significant grid oscillations. By slightly increasing the SGS viscosity at the top, the oscillations are damped out before starting the actual statistical computations. The contours themselves suggest that the granules remain correlated throughout the SAL (which is between 0 Mm and approximately 0.25 Mm). By 1 Mm there is no sign of granulation.

over most of the SAL (between 0 and 0.25 Mm). By the fourth frame there is not much sign of granulation. As the last contour is still more than two pressure scaleheights above the base, the breakup of the granules is probably not caused by the impenetrable bottom boundary. In other words, the bottom boundary is far enough away from the surface. Furthermore, as the shape of the granules does not appear to be influenced by the side walls, the width of the box is also big enough.

The thin closely spaced dark vertical/slanted parallel lines that appear in the first contour, are signs of two grid waves. This is an indication of insufficient damping and is only seen at the very top of the box. It is because of the low SGS viscosity, which is proportional to density (equation 7). This is an undesirable numerical effect. However, as the oscillations occur only at the very top of the box, where the density is very small, their effect on the convection below is minor. Before starting the time integration, we were able to damp out such oscillations, by slightly increasing the viscosity near the top. As these contours only represent one instant in time, such a picture can only provide a limited idea of the nature of the solar granulation. If the same contours are computed at a later time, a completely different picture would be seen. For example, the third frame of Fig. A10 is the same simulation, but the contour was computed 2 solar minutes later.

Clearly, any useful data can only be derived from long time-averaged statistics. One characteristic vertical length-scale associated with convective turbulence is the half-width of the two-point vertical velocity correlation $C[v_z' \; v_z']$. If we assume convective eddies to have an aspect ratio of unity, then this length-scale gives us an idea of the size of the eddies in a turbulent fluid. Using simulation D (described in the appendix), we computed $C[v_z' \; v_z']$ at a series of depths from the top of the box inwards. The results are shown in Fig. 9. From approximately 0 to 1 Mm the eddy size remains close to 600 km. From the beginning to the end of the plateau, both density and pressure have increased by an order of magnitude. Over this range the eddy does not seem to be affected by stratification. However, over the next Mm the eddy size increases to approximately 1100 km. After that the lower boundary starts to influence the eddies. The bends at the far left and far right of the plot signal the approach of the upper and lower boundaries.

The velocity contours and the velocity correlation length both suggest that the granules have some coherent vertical structure. The contours show intergranule lanes that do not shift much between 0 and 0.2 Mm, i.e. the granules are like cylinders. The half-width suggests a vertical size of approximately 600 km, between 1 Mm and the surface. This length-scale does not seem to be affected by the stratification. The strong vertical coherence implies that the convection is dominated by strong downflows that originate close to the surface. SN showed that solar granulation is primarily driven by radiative cooling at the surface. When ascending fluid approaches the surface, it loses heat so rapidly that very strong downflows are created. The downflows are not deflected by the surrounding fluid until they are approximately 1 Mm below the surface, by which point they have weakened enough to be deflected/broken up by the surrounding fluid motion.

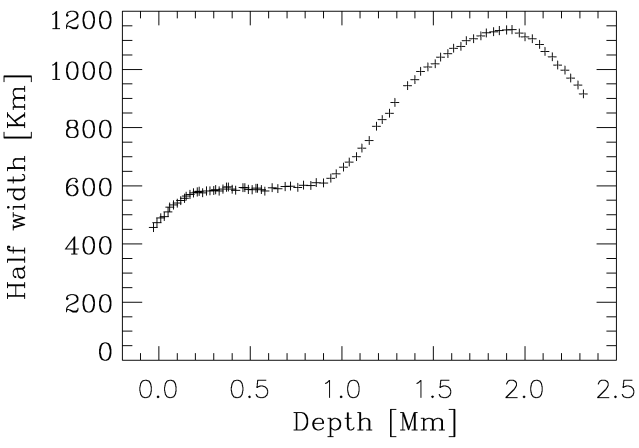

Figure 9. The half-width of the two-point vertical correlation length of vertical velocity at different depths. The right-hand side of the plateau is 3 PSH above the bottom of the box. Between the surface and a depth of 1 Mm, the half-width is nearly constant.

4.4.2 *Heat transport*

In Chan & Sofia (1987, 1989) the two-point vertical velocity and temperature correlations were found to scale with pressure scaleheight rather than density scaleheight. This study was for deep efficient convection. In shallower layers Kim et al. (1995) found that while the vertical velocity correlation scaled with both density and pressure scaleheight, the temperature could not be scaled with either. The difference from Chan & Sofia's results, was caused by the inclusion of the coupling of the partial ionization with convection (they were treated separately by Chan & Sofia). As a fluid parcel moves upwards through regions of decreasing ionization, it liberates ionization energy that increases the buoyancy of the fluid parcel. However, because radiation was modelled by the diffusion approximation (which is known to break down at some point in the SAL), the simulations of Kim et al. could only include the lower half of the SAL.

The present models include all of the SAL. Figs 10 and 11 show $C[v_z' \; v_z']$ and $C[S' \; S']$ at depths of 0.06, 0.2, 0.3, 0.47 and 1 Mm, denoted by solid, small-dashed, dot-dashed, triple-dot dashed and long-dashed lines, respectively. The curves have been centred about their respective maxima. As the plots do not coincide, neither quantity scales with the pressure scaleheight. Furthermore, if density is used rather than pressure, there was no noticeable improvement (not shown).

The width of the $C[v_z' \; v_z']$ distribution decreases between 0.06 and 1 Mm. This is because the width of the geometric

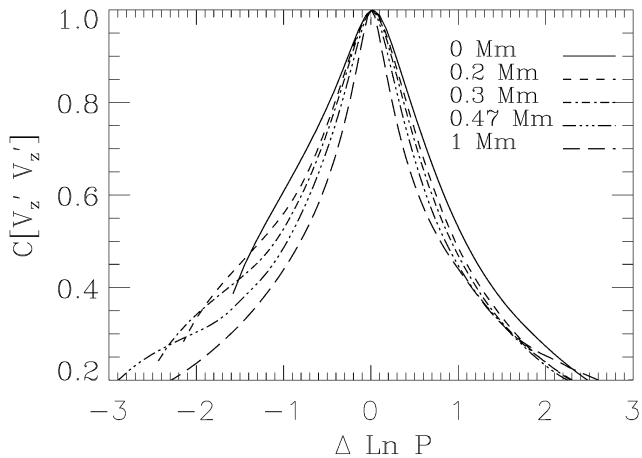

Figure 10. Two-point vertical velocity correlation at five different depths. Unlike the case of deep convection, the velocity correlation does not scale with pressure scaleheight.

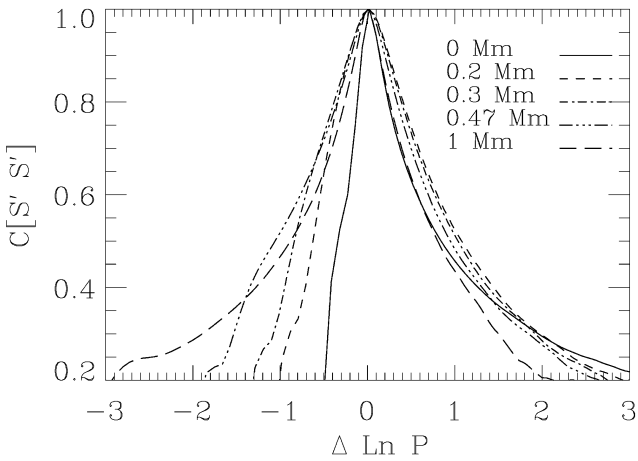

Figure 11. Two-point entropy correlation at the same levels as in the previous figure. Close to the surface, ascending fluid parcels lose their entropy identity much sooner than descending parcels.

distribution is roughly constant (i.e. the half-width is always approximately 600 km, as shown in the previous figure), but the scaleheight increases inwards. The entropy correlation looks very different. For $\Delta \ln P < 0$ the entropy correlation for the three most shallow depths drops rapidly, while for $\Delta \ln P > 0$ it shows a smoother decay. This implies that ascending parcels near the surface, lose heat very quickly, while descending parcels maintain their heat content appreciably longer. Over the last Mm before the surface, the eddies may have approximately the same diameter, but they transport less and less heat as the surface is approached.

This behaviour can be understood by examining the correlation $C[v_z' \; S']$ for upflows and downflows. Fig. 12 shows that the granules are more efficient at transporting entropy downwards than upwards. At the peak of the SAL, $C[v_z' \; S']$ is 0.9 for downflows and 0.6 for upflows. This explains the one-sidedness of $C[S' \; S']$. Consider a fluid parcel that is initially just below the surface (say at a depth of 0.1 Mm). If that parcel moves downwards it will maintain its original entropy for approximately 1 PSH, whereas if the parcel moves upwards it will lose its original entropy in 0.5 PSH. At greater depths $C[v_z' \; S']$ is similar in the upflows and downflows, hence $C[S' \; S']$ is more symmetric deeper down.

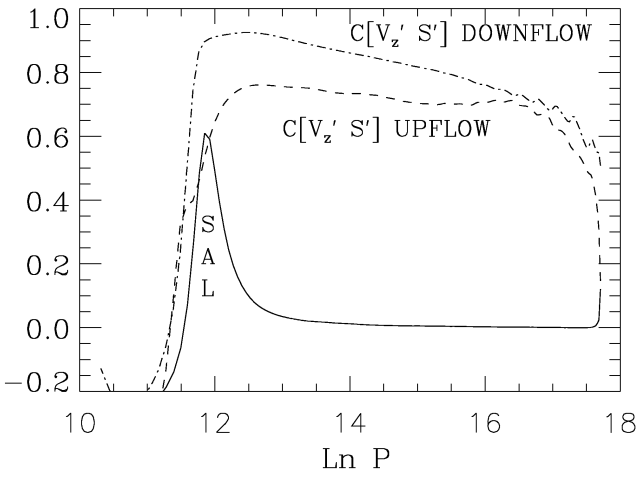

Figure 12. Correlation coefficient between entropy and vertical velocity for upflows and downflows. Also plotted is $\nabla - \nabla_{ad}$ for comparison.

4.4.3 A variable mixing length?

Over the final 1000 km before the surface, the eddies seem to have a nearly constant diameter of approximately 600 km. This would seem to imply a mixing length ratio (the correlation length divided by the pressure scaleheight) that increases towards the surface. However, as the surface is approached, radiation plays a greater and greater role in heat transport, so the mixing length ratio should approach zero at the convection surface. This paradox can be partly resolved by noticing that as the surface is approached, the eddies become less and less efficient at transporting heat upwards. This is shown in the plot of $C[v_z' \; S']$ for the upflows. A more reasonable candidate for the mixing length might be the product of $C[v_z' \; S']$ and the velocity correlation half-width.

5 SUMMARY AND IMPLICATIONS FOR SOLAR MODELS

As we intend to use our code to model the SAL in other stars, this paper is an important benchmark for future studies. From these simulations of the Sun, we found the following.

(i) The impenetrable lower boundary needs to be far enough away from the SAL so that by the time the fluid reaches the boundary, the velocities have become both weak and uncorrelated from velocities in the SAL. If the lower boundary is too close to the SAL, the kinetic energy will be overestimated.

(ii) The horizontal cross-section needs to be large enough so that the side-walls do not restrict the movement of the granules. If the box width is too small then the kinetic energy will be underestimated.

(iii) There is a region close to the surface in which the vertical correlation length remains constant, even though the density and pressure vary by an order of magnitude.

(iv) In that region the mixing length theory, which assumes the correlation length to be a constant multiple of the pressure scaleheight, will not work.

(v) The final equilibrium state is not strictly dependent on the initial model atmosphere (see the Appendix, Section A1).

While these results have been found in a simulation of the Sun, it is reasonable to assume that similar criteria would apply to the convection–radiation transition layers in other stars. The effect of the boundaries should certainly be considered when simulating other convection–radiation layers. The correlation length (half-width) seems to be a very robust feature of the solar granules and could easily be measured in other computations. For example, in a recent proceedings (Robinson et al. 2002) we describe the application of this model to the Sun at the subgiant and the start of the red giant branch. Preliminary results indicate that, near the surface of each convection zone, the ratio of the half-width to the stellar radius depends directly on the surface gravity.

ACKNOWLEDGMENTS

This research is supported in part by NASA grant NAG5-8406 (FJR, PD, SS). YCK is supported by a Department of Astronomy, Yonsei University grant (2001-1-0134). DBG's research is supported in part by a grant from NSERC of Canada. We also would like to acknowledge computer support from the Centre for High Performance Computing at Saint Mary's University in Canada. Finally, we thank H.-G. Ludwig for helpful comments.

REFERENCES

Alexander D.R., Ferguson J.W., 1994, ApJ, 437, 879
Asplund M., Ludwig H.-G., Nordlund Å., Stein R.F., 2000, A&A, 359, 669
Balmforth N., 1992, MNRAS, 255, 603
Basu S., Antia H.M., 1997, MNRAS, 287, 189
Böhm-Vitense E., 1958, Z. Astrophys., 46, 108
Canuto V.M., Mazzitelli I., 1991, ApJ, 370, 275
Cattaneo F., Hurlbert N.E., Toomre J., 1990, ApJ, 349, L63
Chan K.L., Sofia S., 1987, Sci, 235, 465
Chan K.L., Sofia S., 1989, ApJ, 336, 1022
Chan K.L., Wolff C.L., 1982, J. Comp. Phys., 47, 109
Christensen-Dalsgaard J., Berthomieu G., 1991, Solar Interior and Atmosphere (A92-36201 14-92). Univ. Arizona Press, Tucson, p. 401
Demarque P., Guenther D.B., Kim Y.-C., 1997, ApJ, 474, 790
Demarque P., Guenther D.B., Kim Y.-C., 1999, ApJ, 517, 510
Gadun A.S., Hanslmeier A., Pikalov K.N., Ploner S.R.O., Puschmann K.G., Solanki S.K., 2000, A&AS, 146, 267
Guenther D.B., 1994, ApJ, 422, 400
Guenther D.B., Demarque P., 1997, ApJ, 484, 937
Guenther D.B., Demarque P., Kim Y.-C., Pinsonneault M.H., 1992, ApJ, 387, 372
Harvey J.W. et al., 1996, Sci, 272, 1284
Iglesias C.A., Rogers F.J., 1996, ApJ, 464, 943
Kim Y.-C., Chan K.L., 1998, ApJ, 496, L121 (KC)
Kim Y.-C., Fox P.A., Sofia S., Demarque P., 1995, ApJ, 442, 422
Krishna Swamy K.S., 1966, ApJ, 145, 174
Landau L.D., Lifshitz E.M., 1987, Fluid Mechanics, Course of Theoretical Physics, Vol. 6. Pergamon Press, Oxford
Li L.H., Robinson F.J., Demarque P., Sofia S., Guenther D.B., 2002, ApJ, 567, 1192
Lydon T.J., Sofia S., 1995, ApJ, 101, 357
Robinson F.J., Demarque P., Li L.H., Kim Y.C., Sofia S., Guenther D.B., 2002, in Cavallo R., Keller S., Turcotte S., eds, ASP Conf. Ser. 3D Stellar Evolution. Astron. Soc. Pac., San Francisco, in press
Rosenthal C.S., Christensen-Dalsgaard J., Nordlund Å., Stein R.F., Trampedach R., 1999, A&A, 351, 689
Rutten R.J., 1995, Radiative Transfer in Stellar Atmospheres. Available online at www.fys.ruu.nl/~rutten
Smagorinsky J., 1963, Mon. Weather Rev., 91, 99
Steffen M., Gigas D., Holweger H., Krüss A., Ludwig H.-G., 1990, in Stenflo J.O., ed, Proc. IAU Symp 138, Solar Photosphere: Structure, Convection and Magnetic Fields. Kluwer, Dordrecht, p. 213
Stein R.F., Nordlund Å., 1998, ApJ, 499, 914 (SN)
Stein R.F., Nordlund Å., 2000, Solar Phys., 192, 91
Unno W., Spiegel E.A., 1966, PASJ, 18, 85

APPENDIX A:NUMERICAL TESTS

Numerical simulations of solar granulation need to be robust. Part of this means that the walls of the computational box should not control the radiative hydrodynamics of the interior (e.g. the size of the granules, the structure of the SAL, the turbulent pressure, etc.). Nor should any small changes in the initial conditions affect the final equilibrium. The following simulations were designed to minimize these uncertainties.

The features of the individual simulations are summarized in Table A1. In this table the geometric width in both the x and y directions is given in Mm, while the depth is given in Mm and as the number of pressure scaleheights. Models A and B were created by vertically extending model KC2, while C, D and E were made by periodically extending model B. After periodic extension, the horizontal resolution in models D and E was halved. Each time a new model was created, it was allowed to return to thermal equilibrium before the statistical integration was begun.

Table A1. List of simulations.

Model	Width (Mm)	Depth (Mm)	Depth (PSH)	$N_x \times N_y \times N_z$	Δ_x (km)	Δ_z (km)
KC/KC2	1.35	0.9	4.4	60^3	26	17.5
A	1.35	2.1	7.2	$59^2 \times 120$	26	17.5
B	1.35	2.8	8.5	$59^2 \times 170$	26	17.5
C	2.7	2.8	8.5	$116^2 \times 170$	26	17.5
D	2.7	2.8	8.5	$58^2 \times 170$	52	17.5
E	5.4	2.8	8.5	$114^2 \times 170$	52	17.5

For each model we computed three non-dimensional statistical quantities.

(i) The turbulent pressure divided by the mean gas pressure,

$$P^*_{\rm turb} = \bar{\rho} v_z''^2 \big/ \bar{P}, \tag{A1}$$

where the '$*$' denotes a non-dimensional quantity.

(ii) The turbulent kinetic energy per unit mass divided by the isothermal speed of sound squared,

$$\chi^* = \frac{1}{2}\frac{v''^2}{c_{\rm s}^2}, \tag{A2}$$

where $v''^2 = v_x''^2 + v_y''^2 + v_z''^2$ and $c_{\rm s} = \sqrt{\bar{P}/\bar{\rho}}$ is the isothermal speed of sound.

(iii) The superadiabaticity

$$\nabla - \nabla_{\rm ad} = \overline{\frac{\partial \ln T}{\partial \ln P}} - \overline{\nabla_{\rm ad}}, \tag{A3}$$

where $\nabla_{\rm ad}$ is computed using the OPAL equation of state.

From now on we will drop the '$*$' on $P_{\rm turb}$ and χ, for convenience. All quantities in this section are non-dimensional.

A1 The influence of varying the initial conditions

Here we compare the original KC simulation with simulation KC2 listed in Table A1. Both simulations have the same input physics (opacity tables, equation of state). As noted in Section 2.1, the only difference between KC2 and KC, is that the 1D initial models were based on slightly different model stellar atmospheres [i.e. the Eddington $T(\tau)$ relation in KC, versus the empirical Krishna–Swamy $T(\tau)$ relation in KC2]. As the Krishna–Swamy relation is from observations of the Sun, it was closer to the final state of the solar simulation.

Fig. A1 shows the initial hydrostatic (based on the MLT) and relaxed hydrodynamic runs of $\log P$ versus $\log T$ for the two simulations. The dotted and solid lines are the initial plots for KC and KC2, respectively. The horizontal and temporal averages of the relaxed states, are denoted by diamonds and crosses for KC and KC2, respectively. To demonstrate statistical convergence, the data of model KC2 was initially averaged over approximately 600 s of solar surface convection, whereas in KC, the averaging time was 2240 s. After a sufficient amount of time, KC2 (crosses) converged to KC (diamonds). The MLT provides the initial thermal structure, but the hydrodynamical turbulence shapes the final structure. Provided the initial conditions are not too different, the hydrodynamics converges to the same equilibrium state.

This is an important preliminary result. Even if the initial atmospheres are slightly different, the hydrodynamics dictates the final equilibrium. The thermodynamics of the resulting 3D simulation does not depend on the precise details of the MLT. The final equilibrium is not determined by the exact value of the mixing length

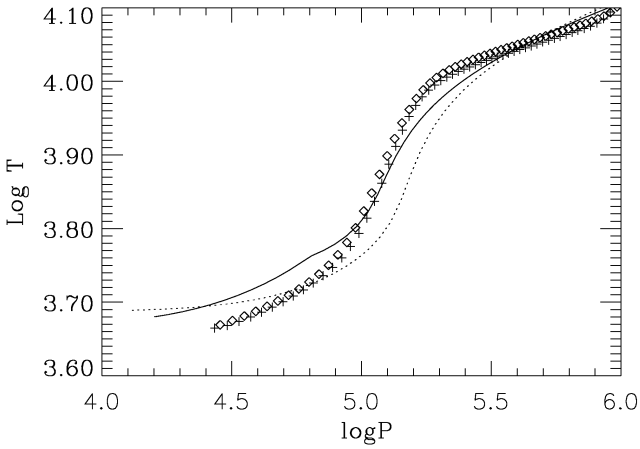

Figure A1. Hydrostatic structure of two 1D stellar models (see the text) for KC (dotted) and KC2 (solid). The mean thermal structure from the hydrodynamic simulations is also shown for KC (diamonds) and KC2 (crosses). Despite different initial stellar models, the turbulence causes both models to eventually converge to the same equilibrium state.

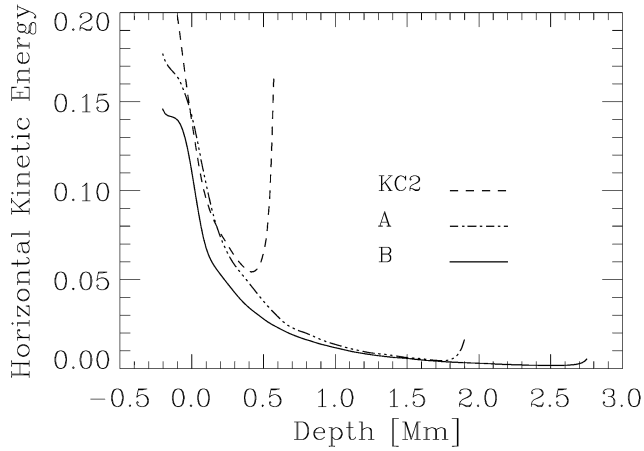

Figure A2. Non-dimensional horizontal turbulent kinetic energy per unit mass, for simulations of different depths. Note the speeding up of the flow at the lower stress-free boundary in KC2.

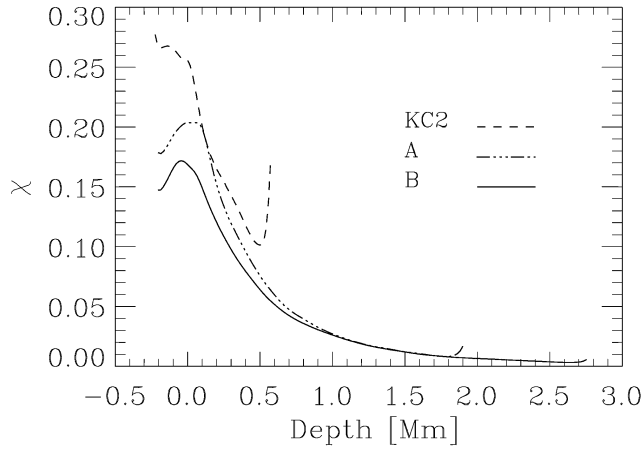

Figure A3. Non-dimensional turbulent kinetic energy per unit mass, χ for simulations of different depths.

ratio in the stellar model, on which the initial state of the simulation is based. The choice between the two initial conditions in the atmosphere, does not affect the turbulent pressure, turbulent kinetic energy or the superadiabatic temperature gradient. These quantities will depend on the geometry and grid resolution in the box.

A2 The influence of the lower impenetrable boundary

The structure of the SAL in KC2 (or KC, which is identical) is at odds with the SAL constructed with the Canuto–Mazzitelli (1991) approach (see fig. 1 in Demarque et al. 1999) or presented in the numerical simulation by Rosenthal et al. The most obvious difference is that KC2 predicts a broader SAL with a maximum of approximately 0.4, while Canuto–Mazzitelli predicts a peak of approximately unity and Rosenthal et al. a peak of 0.6. The height of the peak is related to the convective efficiency with respect to radiative heat transport.

Models KC2, A and B differ only in their domain depths. Simulation A was constructed by adding three extra pressure scaleheights to the base of model KC2 (see Table A1). We first thermally relaxed the lower layer, because with only hydrostatic support (no turbulent pressure), the overlying layer collapsed, and the simulation crashed. Also, when joining the two layers, the turbulent viscosity was temporarily increased. This smoothed out the fluctuations that were produced by suddenly removing the lower boundary. Model B was made by adding a hydrostatic layer computed using the MLT to model A. This increased the depth from 2.1 to 2.8 Mm. As the turbulent pressure near the bottom of model A was small (approximately 1 per cent of the gas pressure), in this case we did not need to relax the hydrostatic lower layer separately.

A.2.1 Effect on kinetic energy and turbulent pressure

To demonstrate the effect of the lower boundary on the turbulent flow, we computed the ratio of the horizontal kinetic energy to the gas pressure. This is equivalent to the horizontal turbulent Mach number squared, i.e.

$$\chi_{\rm horiz} = \frac{1}{2}\bar{\rho}\left(v_x''^2 + v_y''^2\right)/\bar{P} = \frac{1}{2}\left(v_x''^2 + v_y''^2\right)/c_s^2. \qquad \text{(A4)}$$

Fig. A2 shows $\chi_{\rm horiz}$ for models KC2, A and B. In KC2 the magnitude of $\chi_{\rm horiz}$ shoots up at the base. The net effect of the fast downflows striking the lower boundary was to speed up the overall flow. This increased the total turbulent kinetic energy χ throughout the box (Fig. A3).

The upturn near the bottom of each layer, is clearly reduced as the boundary is moved deeper, and is almost eliminated when the depth is 2.8 Mm. This problem is much less severe at the top boundary because the underlying region is subadiabatic (the radiative zone). The vertical velocity is already small when the flow hits the top boundary. The effect on $P_{\rm turb}$ of moving down the lower boundary is shown in Fig. A4. In model KC2, $P_{\rm turb}$ drops sharply as the impenetrable bottom is approached. While for A and B it has a much smoother decay.

A.2.2 Effect on superadiabaticity

The run of $\nabla - \nabla_{\rm ad}$ for the MLT, and models KC2, and C was shown previously in Fig. 4. When the SAL is moved outwards by turbulent pressure, the convective efficiency is reduced and radiation is forced to carry more of the total flux. This should result in an increased

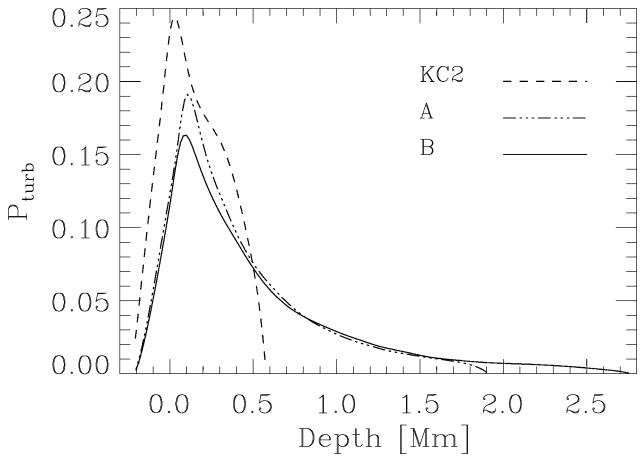

Figure A4. Ratio of turbulent pressure to gas pressure, in this case denoted by P_{turb}, for simulations of different depths.

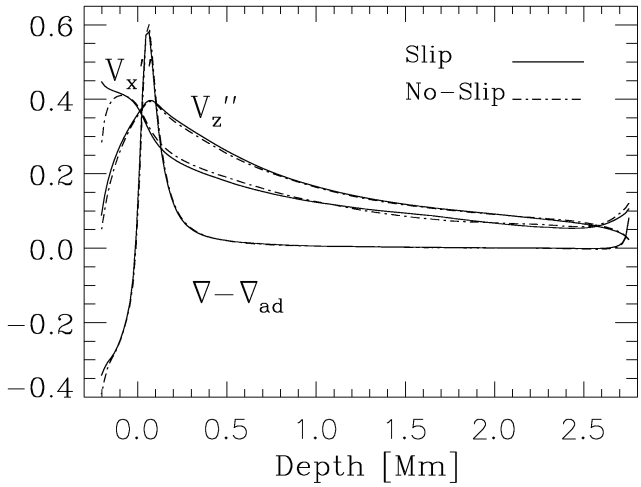

Figure A5. Model D with a slip (stress-free) and a no-slip top boundary. The figure includes horizontal and vertical turbulent velocities and superadiabaticity. The velocities have been scaled by the local speed of sound.

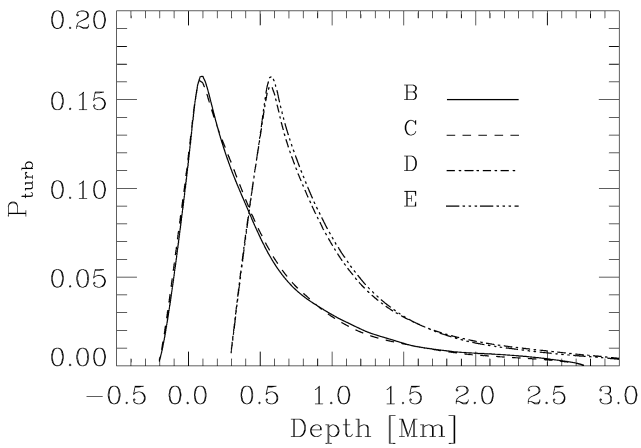

Figure A6. Turbulent pressure as a function of domain width. P_{turb} is the ratio of the turbulent pressure to the gas pressure. The plot for D and E has been shifted by 0.5 Mm for clarity. Without the shift the peaks would coincide.

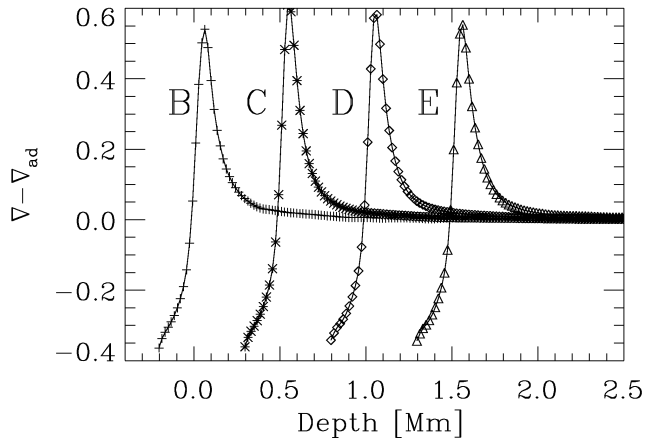

Figure A7. Superadiabaticity as a function of domain width for models B, C, D and E. The vertical grid points are individually marked to show that the SAL is well resolved. The plots have been spaced by 0.5 Mm for clarity. Without the horizontal spacing all the plots would have zero superadiabaticity at a depth of 0 Mm.

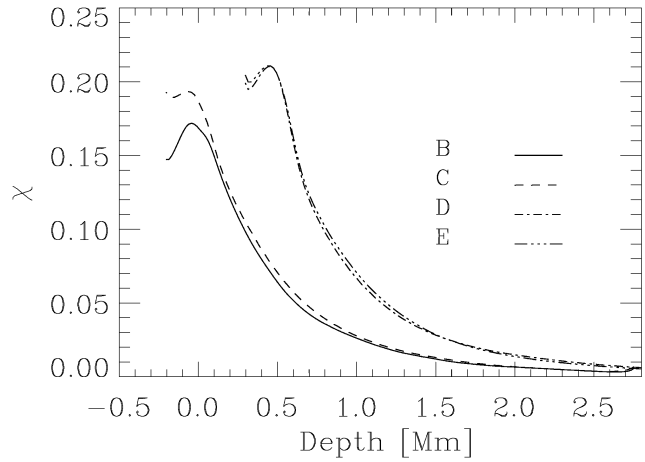

Figure A8. Non-dimensional turbulent kinetic energy for different domain widths. The plot for D and E has been shifted by 0.5 Mm for clarity.

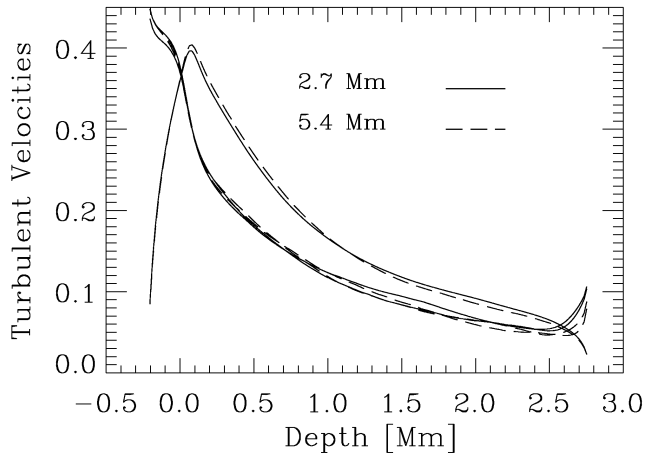

Figure A9. The three components of turbulent velocity (scaled by the isothermal speed of sound), for simulations D and E. As the change in width has little effect on any component of the velocity, 2.7 Mm seems to be a sufficient box width.

height of the SAL compared with the MLT. However, in KC2 the convection is overly turbulent and is thus (incorrectly) more efficient than convection computed via the MLT. This results in a drop in the height of the SAL compared with the MLT.

A3 The influence of the upper impenetrable boundary

As the top boundary is also impenetrable we need to ensure that its position does not effect the convection either. We need to prove that decreasing vertical velocity between the convection surface (where the depth = 0 Mm) and the top of the box, is not caused by the top boundary. Rather it should be as a result of the stable layer at the top, i.e. convection–radiation losses.

To address this issue we damped the horizontal velocity at the top by replacing the stress-free boundary with a no-slip top. The flow is then relaxed and statistics are gathered as usual. Fig. A5 shows $\nabla - \nabla_{\rm ad}$, v_x'' and v_z'' for simulations with slip and no-slip top boundaries. The velocities are non-dimensionalized by the local isothermal speed of sound. This conveniently enables them to be on the same axis as $\nabla - \nabla_{\rm ad}$. Apart from the top 100 km, where the two v_x''s diverge because of the different top boundary conditions, the rms vertical and horizontal velocities are nearly the same for the no-slip and stress-free top boundaries. This implies that the drop in vertical velocity near the top is primarily caused by convection to radiation losses, rather than the top boundary. Furthermore, the horizontal velocity in the upper atmosphere does not affect the SAL structure much (i.e. $\nabla - \nabla_{\rm ad}$).

A4 The influence of the domain width

Models B, C, D and E have widths of 1.35, 2.7, 2.7 and 5.4 Mm, respectively. To judge the effect of width on simulations without changing the grid spacing, we should compare B–C and D–E. All four models have similar $P_{\rm turb}$ and $\nabla - \nabla_{\rm ad}$ (Figs A6 and A7). Increasing the width seems to have a minor effect on either $P_{\rm turb}$ or $\nabla - \nabla_{\rm ad}$. In general, it is essential to resolve turbulent motions inside the SAL region. As this is only approximately 250 km thick, the grid spacing in the SAL needs to be very small. To show that all of our simulations have resolved the SAL, we have plotted the individual vertical grid points in the figure.

The variation of χ with domain width is more interesting. This is shown in Fig. A8. When the width is increased from 1.35 to 2.7 Mm, χ increases (especially near the top). However, when the width is increased from 2.7 to 5.4 Mm there is only a very small change in χ. A box width of 2.7 Mm seems to be sufficient to resolve χ for solar granules.

To provide further evidence that 2.7 Mm is a large enough box width, we computed v_x'', v_y'' and v_z'' for models D and E. Fig. A9 shows all three velocity components for both D and E. Doubling the width has only a minor effect on any particular velocity component. The small differences in the deeper part, are caused by insufficient convergence. As the domain has periodic lateral boundaries, eventually the horizontal velocities should all be the same.

Fig. A10 shows contour plots of the instantaneous vertical velocity, for a horizontal cross-section, for models of different widths. The uppermost frame shows that not even a single granule can fit in the box when the width is 1.35 Mm, while approximately two fit easily into the box in the second frame. In the final frame approximately nine or ten larger cells fit into the box. Owing to computational restrictions the final figure is computed on a coarser mesh than the previous three frames so the granules are not clearly depicted.

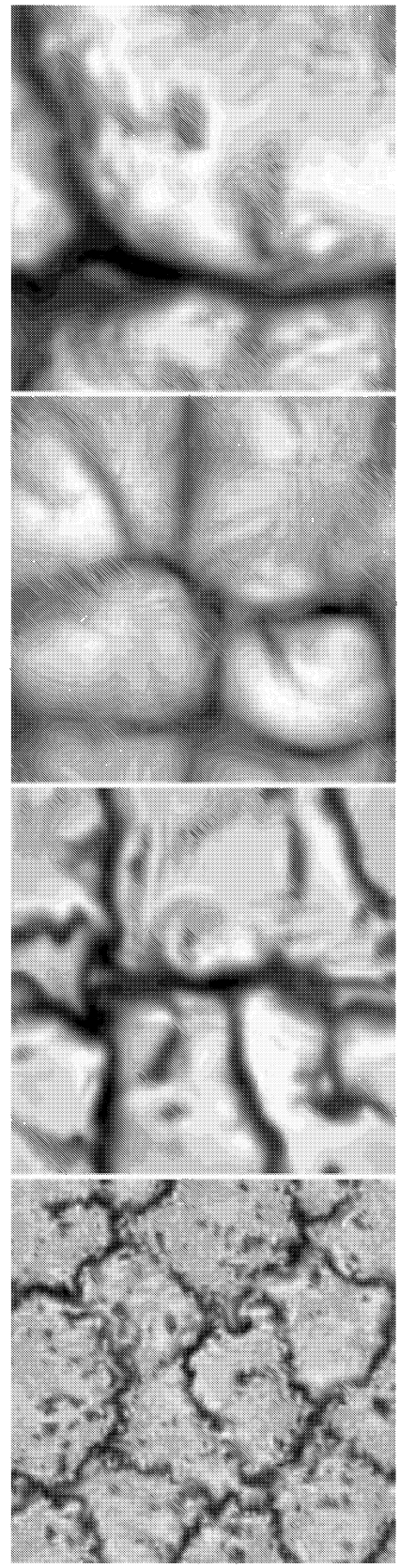

Figure A10. Snapshot of vertical velocity contours for different domain widths. From top to bottom the domain widths are 1.35, 2.7, 3.75 and 5.4 Mm, respectively. Owing to computational restrictions the final frame has half the resolution of the other three.

A5 The influence of numerical resolution

While the main point of these tests is to show that the walls of the computational box can have a significant effect on granular convection, we can also partially address the effect of changing the horizontal grid spacing. Models C and D produced very similar $P_{\rm turb}$ and $\nabla - \nabla_{\rm ad}$, while χ differed only slightly. As χ depends on the horizontal and the vertical velocity, this probably reflects the sensitivity of the horizontal component of kinetic energy to horizontal grid resolution. This is particularly noticeable near the top where the flow is mostly horizontal.

This paper has been typeset from a TEX/LATEX file prepared by the author.